Journal of Environmental Chemical Engineering 11 (2023) 111072

Contents lists available at ScienceDirect

Journal of Environmental Chemical Engineering

journal homepage: www.elsevier.com/locate/jece

Effect of the synthesis method on the performance of Ni-CeO_2-ZrO_2 catalysts for the hydrogenolysis of glycerol with endogenous hydrogen

N. Vera-Hincapie [a], U. Iriarte-Velasco [b], J.L. Ayastuy [a,*], M.A. Gutiérrez-Ortiz [a]

[a] Department of Chemical Engineering, Faculty of Science and Technology, University of the Basque Country (UPV/EHU), Sarriena S/N, 48940 Leioa, Spain
[b] Department of Chemical Engineering, Faculty of Pharmacy, University of the Basque Country (UPV/EHU), Paseo de la Universidad 7, 01006 Vitoria-Gasteiz, Spain

ARTICLE INFO

Editor: Chao He

Keywords:
Glycerol
Nickel
Ceria-zirconia
Aqueous-phase reforming
Hydrogenolysis
Endogenous hydrogen

ABSTRACT

In this work, we investigated the influence of the synthesis method of Ni-based CeZr catalysts on their physicochemical and catalytic properties in the hydrogenolysis (HDO) of glycerol with H_2 in-situ produced by the aqueous-phase reforming (APR). Conventional impregnation method involved surface nickel deposition (NiCeZr-IM). The one-pot methods, which involved nickel embedment into CeZr lattice, included sol-gel (NiCeZr-SC) and coprecipitation (NiCeZr-CA and ultrasound-assisted NiCeZR-CS) methods. Differences in textural, structural, morphological, redox, and surface properties, together with and catalytic performance in the glycerol APR-HDO, were investigated systematically. As well, spent catalysts were deeply characterized. There were notable differences among textural properties, which significantly affected their activity in glycerol conversion. The structural characterization confirmed the successful integration of Ni into the CeZr lattice, especially for the catalysts synthesized using one-pot methods. One-pot synthesized catalysts showed stronger Ni-CeZr interaction, which affect the reducibility. The catalysts prepared by coprecipitation contained the highest metal-to-acid ratio, making them very active for C-O bond hydrogenation. Post-reaction characterization discloses a leaching of the nickel, in greater amount for both coprecipitated catalysts. This study revealed the potential of Ni-based catalysts derived from subsurface insertion of nickel into the CeZr matrix for the hydrogenolysis of glycerol without external hydrogen.

1. Introduction

The use of fossil fuels is considered the leading cause of global warming. The alternative is the use of renewable and sustainable energy sources, where solar, wind, geothermal and biomass are some of the most promising solutions. Biomass offers a unique advantage as renewable feedstock for the production of different value-added chemical products, contributing to the decarbonization and to the circular economy. Glycerol, one of the DOE's 12 top biobased building block, is a by-product of the transesterification of triglycerides to produce biodiesel [1]. The continuous increase in the production of glycerol results in a huge surplus in its stocks, making it an attractive raw material for the biorefinery. The high degree of functionality of glycerol means that various processes can be employed for its valorization [2]. One such example of glycerol transformation to useful chemicals is its selective hydrogenolysis, also known as hydrodeoxygenation (HDO) to propanediols. HDO holds a potential to bridge current fossil technologies and future biomass refinery processes [3]. The HDO process involves C–O bond cleavage and subsequent addition of hydrogen [4], for which bifunctional catalysts are needed.

The use of external hydrogen presents some important drawbacks, such as safety issues of working at high pressures, the low solubility or its fossil sources origin [5]. In-situ hydrogen production and simultaneous use in the hydrogenolysis can overcome these drawbacks. In this one-pot system, in-situ H_2 production is made by reforming of a part of glycerol by the Aqueous-Phase Reforming (APR), consisting in the preferential C–H and C–C bond cleavages to produce H_2 and CO_2. This H_2 is then employed to C–O bond cleavage of the intermediate of the glycerol dehydration to form propanediol [6]. Therefore, an effective catalyst for the APR coupled to HDO should be active in both C–H and C–C, and in C–O bond scission.

A variety of metals have been used for the APR and for the hydrogenolysis, such as noble metals [7], transition metals such as Co [8], Cu [9] or Ni [10], and bimetallic [5]. In most cases, they are supported on different oxides such as Al_2O_3, ZrO_2, CeO_2, TiO_2, SiO_2, and activated carbon [11,12], but also they are used mixed oxides as precursors of the

* Corresponding author.
E-mail address: joseluis.ayastuy@ehu.eus (J.L. Ayastuy).

https://doi.org/10.1016/j.jece.2023.111072
Received 27 July 2023; Received in revised form 7 September 2023; Accepted 19 September 2023
Available online 21 September 2023

catalysts [13,14].

Nickel, usually used for APR and hydrogenolysis since it is inexpensive, favours methanation, thus reducing the hydrogen production. Moreover, Ni tends to oxidize and sinter under hydrothermal conditions [15]. Therefore, Ni-based catalysts must be synthesized elaborately to be real alternative to noble metals for APR and HDO applications.

Ni/CeO_2 shows great potential to be used in the APR of glycerol [16], attributed to the high oxygen mobility which promote preferentially the WGS versus the methanation reaction and, thus, enhanced hydrogen production [17]. The redox capacity and hydrothermal resistance of ceria can be enhanced by doping with Zr [18].

Ni-based catalysts with ceria-zirconia mixed oxides have been predominantly used in the steam reforming of oxygenated molecules [19]. Their application in the aqueous-phase transformation of glycerol is not as extensive but is gaining momentum [20]. In the specific context of the glycerol APR, bimetallic PtNi catalysts, prepared by impregnation and supported on $CeZr\text{-}Al_2O_3$, have been employed and were found to demonstrate remarkable performance in the liquid-phase conversion of glycerol [21]. Bastan et al. [22] examined the impact of altering the cerium composition on the glycerol APR activity of $Ni/Ce_XZr_{1-X}O$ catalysts. Their results revealed that ceria itself exerts a considerable effect on the catalyst's activity and reaction stability.

Preparation method can influence the physicochemical properties (i.e., crystallite size, reducibility, metal dispersion, acidity) of the catalyst [23]. It has been found that the method of synthesis of the Ni-CeZr catalyst has a great influence on the dispersion of the active phase and its interaction with the support. Various method have been applied to the synthesis of Ni-Ce-Zr catalysts [23], among others incipient wetness impregnation [24], sol-gel [25], co-precipitation [26], and combustion [27]. Some of these methods manage to embed the Ni in the lattice, while others do not.

To our knowledge, there are no comprehensive comparative studies investigating the different synthesis methods impact on the features and efficacy of CeZr-supported nickel catalysts in the APR coupled to HDO of glycerol. Therefore, this study deals with the effect of the preparation method on the physico-chemical and catalytic properties of NiCeZr catalysts. In this study, we synthesized NiCeZr catalysts via four synthesis methods, either by surface deposition of nickel or by embedding nickel in the subsurface of the ceria-zirconia mixed oxide, in order to obtain solids with different Ni-CeZr interaction strengths. The obtained catalysts were thoroughly characterized, either in the fresh and reduced form, in order to correlate the physico-chemical properties with the catalytic performance. In addition, exhausted catalysts were also characterized to gain knowledge in the main deactivation causes.

2. Experimental

2.1. Synthesis of materials

A series of nickel and ceria-zirconia catalysts (NiCeZr) were synthesized with a nominal composition 10 wt% Ni and Ce/Zr= 0.15/0.85 (mol/mol) ratio. In order to vary the nature of interaction between nickel and cerium-zirconium precursors, four synthesis methods were used. Detailed synthesis procedures are given in ESI. In short, NiCeZr-IM was synthesized by impregnation of nickel over CeZr (previously synthetized by coprecipitation with ammonia aqueous solution, using cetyltrimethylammonium bromide –CTBA– as surfactant). NiCeZr-SC solid was synthesized using one-pot sol-gel method, using citric acid as chelating agent. NiCeZr-CA and NiCeZr-CS solids were synthesized by one-pot coprecipitation with NaOH, without and with ultrasonic irradiation, respectively, and using CTBA as surfactant. All the solids were calcined at 500 °C for 4 h (heating ramp 1 °C/min) in a muffle.

2.2. Characterization of materials

Bulk chemical composition of the solids was analysed by ICP-AES, while leached metals were quantified by ICP-MS. Textural properties of the solids were evaluated from N_2 adsorption-desorption isotherms at 77 K. The specific surface area and the main pore size were determined with the BET and BJH (adsorption-branch) methods, respectively.

XRD of the solids in powder form were collected using monochromatized CuKα radiation. The crystallite size was calculated by Scherrer equation. Identification of the crystal phases was carried out on the basis of ICDD database.

H_2-TPR was carried out on the solid previously cleaned by He flow at 500 ºC. The analysis was carried out by rising the sample temperature into 5% H_2/Ar stream up to 900 °C at 10 °C/min, monitoring the signal by TCD. The metallic surface was evaluated by H_2 chemisorption at 5 ºC to circumvent H_2 spillover, using double isotherm method. The difference between the first and second isotherms was taken as the chemisorbed H_2.

To further study the morphology of the reduced catalysts, scanning transmission electron microscopy (STEM) equipped with an energy-dispersive X-ray spectroscopy (EDX) detector was used.

Ammonia chemisorption and NH_3-TPD was carried out on the reduced catalysts. First, to quantify the chemisorbed quantity a series of six pulses of 10% NH_3/He were introduced at 90 °C. After evacuation for 60 min, NH_3-TPD was done ramping the sample temperature up to 900 °C at a heating rate of 10 °C/min, in He flow.

Raman spectra were recorded with laser of 514 nm in the 150–1500 cm^{-1} spectral window. The UV–vis–NIR DRS spectra, collected in 200–2500 nm range, were transformed to the Kubelka-Munk function.

The oxidation state of surface metals was studied by XPS (Al Ka, 1486.7 eV, X-ray radiation) in both calcined and reduced form of catalysts. The peaks were deconvoluted after Shirley background subtraction, using a mixed Gaussian–Lorentzian function. More details on analytical methods are given in ESI.

2.3. Catalytic tests

The reaction was performed in a tubular reactor (Microactivity Effi, PID Eng&Tech) at 235 °C and 35 bar, operating at WHSV = 12 h^{-1} (0.50 g of catalyst with 0.04–0.16 mm particle size), feeding 10 wt% glycerol aqueous solution (0.12 mL/min flow), over catalyst in-situ reduced at 600 ºC for 1 h. The reactor was pressurized with He up to the desired pressure, then the He flow was switched to bypass, and the liquid feedstream pumped into the reactor while the temperature was progressively raised at 5 ºC/min up to the reaction temperature. Zero time was taken when reactants reached the catalyst bed, once ensured the reaction temperature was reached. Catalytic performance was measured at 3 h TOS. Gaseous and liquid products were separated in a Peltier device at 5 ºC. The gaseous products were online analyzed by μGC (Agilent 490) equipped with four columns (Al_2O_3-KCl, PPQ and MS5A columns that used He as a carrier, and MS5A column which used Ar as a carrier). The liquid product was collected every hour in vials and off-line analyzed by GC-FID (Agilent 6890 N, DB-Heavy Wax column). The carbon content in the liquid phase was measured on a Shimadzu TOC-L apparatus. The carbon balance was above 90% for all the experiments. Both the gas and liquid products were quantified by external calibration.

2.4. Equations used for calculations for catalytic results

Glycerol conversion (X_{Gly}) was calculated according to:

$$X_{gly}(\%) = 100 \times \frac{F_{gly}^{in} - F_{gly}^{out}}{F_{gly}^{in}} \quad (1)$$

where F_{gly}^{in} and F_{gly}^{out} are the glycerol molar flow at the reactor inlet and outlet, respectively. The yields of gas and liquid products were calculated on carbon basis, as follows:

$$Y_{gas}(\%) = 100 \times \frac{F^{out}_{C,gas}}{3F^{in}_{gly}} \quad (2)$$

$$Y_{liq}(\%) = 100 \times \frac{F^{out}_{C,liq}}{3F^{in}_{gly}} \quad (3)$$

$F^{out}_{C,gas}$ and $F^{out}_{C,liq}$ are the total molar flow of C in the outlet gas and liquid stream (excluding glycerol), respectively.

For the C-containing products, selectivity (S_i) to product i was calculated on carbon basis, as follows:

$$S_i(\%) = 100 \times \frac{F^{out}_{C,i}}{F^{out}_{C,phase}} \quad (4)$$

where $F^{out}_{C,phase}$is the total C flow in all the analysed products in the same phase as product i. Hydrogen yield (Y_{H2}) was the ratio between the produced H_2 and the ideally produced by glycerol APR:

$$Y_{H_2}(\%) = 100 \times \frac{1}{7} \times \frac{F^{out}_{H_2}}{F^{in}_{gly}} \quad (5)$$

3. Results and discussion

3.1. Textural properties and bulk chemical composition

The nickel content in the bulk is summarized in Table 1, while Table S1 (ESI) contained the content of other elements of the calcined solids. For all the solids, the targeted Ce/Zr ratio was achieved. Ni loading varied with the synthesis method, and except for NiCeZr-CS, it was lower than nominal. The coprecipitation methods led to defective Ni loading, probably due to the slower precipitation kinetics of nickel [28], which could have been removed as Ni^{2+} during the washing steps. Both solids prepared by coprecipitation contained traces of sodium.

In the calcined form, the materials presented type IV isotherms (Fig. S1A, ESI), characteristic of mesoporous solids. NiCeZr-SC showed type H4 hysteresis cycle, characteristic of aggregates of plate-like particles and partially filled macropores. The other three materials showed H2(b) hysteresis type, typical from complex system of pores where the pore neck is narrower than the body. All the solids, in their calcined form, showed unimodal pore size distribution (PSD) (Fig. S1B, ESI). NiCeZr-SC and NiCeZr-CA catalysts showed the narrowest PSD, with maxima at around 3.4–3.9 nm. Contrarily, catalysts NiCeZr-IM and NiCeZr-CS contained larger pores and a wider PSD, with its maxima at around 4.6 nm.

Ni loading by impregnation onto the CeZr support decreased the specific surface area (S_{BET}) and pore volume (V_{pore}) by 22% and 16%, respectively (Table 1), suggesting that Ni particles blocked small pores. In the calcined form, the S_{BET} varied significantly with the synthesis method, between 52.1 m^2/g (NiCeZr-SC) and 282.3 m^2/g (NiCeZr-CA). It is worth noting that both solids prepared by coprecipitation showed oustanding S_{BET} (between 3 and 5.4 times larger than others), what could be ascribed to the use of a soft template (CTBA) that facilitated an orderly growth of nanoparticles. Moreover, the removal of the soft template during the washing of the slurry could protect from the collapse of the material structure [29]. The notably lower S_{BET} and pore volume of NiCeZr-SC solid suggested collapse of its porous structure, promoted by the removal of the crosslinking agent (citrate) by heating. The significantly larger S_{BET} of catalysts NiCeZr-CA and NiCeZr-CS could be attributed to the use of CTBA and to the distortion generated in the tetragonal unit cell of the CeZr lattice (discussed below). Also, the effect of the used precipitant agent (NaOH vs ammonia) in the pore structure of the as-obtained solids should not be discarded.

In their reduced forms, catalysts NiCeZr-IM and NiCeZr-SC preserved their structural integrity, as the S_{BET} and V_{pore} were hardly varied. On the contrary, the S_{BET} of NiCeZr-CA and NiCeZr-CS solids decreased by c. a. 20% with respect their calcined forms. The PSD of the other solids varied upon reduction. In the case of catalyst NiCeZr-IM, the average pore size increased from 4.6 to 5.2 nm. For NiCeZr-CS and NiCeZr-CA solids, a bimodal PSD could be deduced, with contribution at 3.8 and 5.0 nm).

3.2. Structural characteristics

The XRD profiles of the fresh solids are shown in Fig. 1A. The diffractogram of reference CeZr corresponded to ceria-zirconia solid solution (PDF 88–2398). Due to the low crystallinity of the support, it was difficult to distinguish among the tetragonal and cubic structures [30]. However, results from Raman analysis (below) suggested that both phases existed in our solids. Previous works report that in cerium-doped zirconia solids tetragonal phase predominates for cerium content below 40% [31]. No characteristic peaks from zirconia or ceria single phase were detected, indicating neither of both was segregated. Both catalysts prepared by coprecipitation exhibited broader and less defined XRD peaks suggesting they contained smaller crystallites and were more amorphous.

After impregnation of nickel, XRD peaks from cubic NiO (JCPDS 01–078–0643) were detected indicating the presence of NiO entities at the periphery of the particles. Among the one-pot synthesized catalysts, NiCeZr-CS and NiCeZr-SC exhibited the weakest NiO diffraction peaks, what indicated a higher dispersion of NiO. Perfectly dispersed NiO could be deduced for NiCeZr-CA due to the absence of XRD signals. An attempt was done to determine the effect of Ni solution in the CeZr lattice, assuming tetragonal lattice for the solid solution (JCPDS 01–088–2398). The lattices variation with the synthesis method (Fig. 1C) indicated that both *a* and *c* lattice lengths varied upon addition of nickel, consistent with the difference in the ionic radii of Ni^{2+} (0.69 Å) with respect to Zr^{4+} (0.84 Å) and Ce^{4+} (0.97 Å). Upon Ni doping, the lattice shrunk in the *c*-axis whereas expanded in the *a*-axis. The method of Ni loading strongly affected to the variation in lattices lengths, which suggested that the synthesis method influenced in the Ni-CeZr intimacy. Note that the *c*/*a* ratio (labelled in the Fig. 2C), which is an indicator of the distortion of the tetragonal unit cell, hardly varied upon nickel doping (< 3%), except for NiCeZr-CS solid, which produced a much pronounced distortion (c.a. 11%) of the tetragonal lattice. Both, the charge imbalance in the lattice due to Ni^{2+} solution, and the distortion because of the size difference between Ce^{4+} and Zr^{4+} usually generate vacancies in the lattice [32]. In summary, the synthetized solids, instead of a ternary solid solution, showed a hetero-structure system with NiO particles supported onto oxygen-deficient NiCeZr solid solution.

Table 1
Physico-chemical properties of the NiCeZr-X series.

Catalyst	Ni (%)	S_{BET} (m^2/g)	$d_{NiCeZr,XRD}$[a] (nm)	$d^b_{NiCeZr,BET}$ (nm)	d_{NiO}[a] (nm)	$d^a_{Ni^0}$ (nm)	E^c_g (eV)	Ni sites × 10^{-19d} (sites/g_{cat})	Ni dispersión[d] (%)
CeZr	0.0	105.5 (n.a.)	5.7 (n.a.)	9.3 (n.a.)	n.a.	n.a.	3.1	n.a.	n.a.
NiCeZr-IM	9.0	82.6 (81.7)	5.5 (5.4)	11.9 (12.0)	18.6	47.0	3.2	1.26	2.7
NiCeZr-SC	10.0	52.1 (54.9)	4.7 (6.0)	18.9 (17.9)	5.6	62.5	2.7	1.25	2.4
NiCeZr-CA	7.8	282.3 (221.1)	2.6 (2.6)	3.5 (4.1)	n.d.	30.1	3.0	1.06	2.6
NiCeZr-CS	9.2	234.6 (189.7)	2.2 (3.9)	3.9 (4.5)	7.3	46.0	2.9	1.95	4.1

[a] from XRD; [b] using $d_{BET} = 6000/(\rho \cdot S_{BET})$ equation, taking $\rho = 6.1$ g/cm^3; [c] band gap energy from DRS; [d] from H_2 chemisorption; n.d.: not detected; n.a.: not analyzes. Values in parenthesis correspond to the reduced form of the solids.

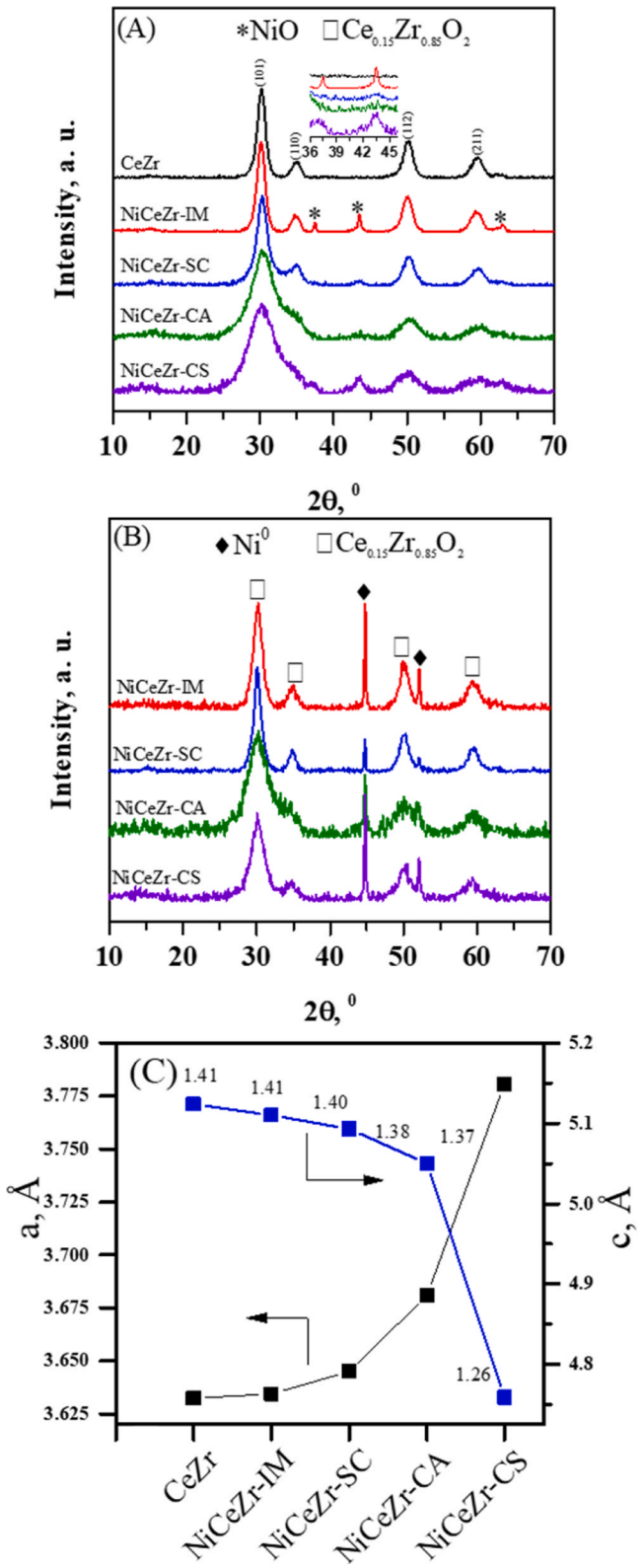

Fig. 1. XRD profiles of the (A) calcined and (B) reduced solids, and (C) lattice parameters for calcined solids.

The solid solution phase was fully retained upon reduction (Fig. 1B), with absence of separated ceria phases. The diffraction peaks from NiO vanished and new, sharp peaks ascribed to metallic nickel (JCPDS 01–087–0712) emerged. These results suggested that the thermal reductive treatment at 600 °C induced in-situ growth of Ni particles attached onto the CeZr surface though Ni ex-solution from the NiCeZr solid solution [33].

For all the calcined solids, the crystallite size of the NiCeZr phase was below 5.5 nm (Table 1). The outstanding small domains for NiCeZr-CA and NiCeZr-CS solids (two-fold smaller) suggested that the usage of CTBA leaded to the inhibition of crystal growth, consistent with their high S_{BET} [34]. The above-mentioned contraction in the *c*-axis could be involved.

Upon reduction, the crystallite sizes of the solid solutions were little modified. The solid particles were bigger than crystallites (size calculated from S_{BET} bigger than size calculated from XRD), indicating particles formed by aggregation of crystallites. Thus, the highest S_{BET} of both solids prepared by coprecipitation (3–5 times higher than the others) could be attributed to the lower aggregation degree of crystallites. For all the catalysts, the NiO crystallite size was smaller than the size of Ni^0 (difference above 28 nm) produced upon reduction, evidencing coalescence of Ni^0. Among the one-pot synthesized solids, those prepared by coprecipitation showed less increase, indicating that their Ni^{2+} species bonded more strongly to CeZr surroundings. The Ni^0 crystallites ranged between 30 nm (NiCeZr-CA) and 62 nm (NiCeZr-SC).

Further characterization of the structure of the solids was carried out by Raman spectroscopy (Fig. 3).

Bare CeZr showed four main Raman bands. Bands at 245, 309 and 453 cm^{-1} were characteristics of tetragonal phase [35], while the band at 619 cm^{-1} was ascribed to cubic phase [30]. Upon nickel impregnation, new band emerged at around 520 cm^{-1}, attributed to bulk NiO [36], consistent with XRD. Among the one-pot synthesized solids, the spectrum of NiCeZr-IM showed the biggest semblance with that from CeZr. The other solids showed less defined spectra with wider peaks, which pointed to smaller NiO entities [37], in agreement with XRD. All these features indicated a composite character of the solid.

After reduction, all the materials showed a similar profile of Raman spectra, composed by a broad band. The contribution from passivated NiO layer on the surface of metallic nickel should not be discarded.

The electronic structure of the surface elements of NiCeZr solids was also investigated by DRS UV-Vis-NIR spectroscopy (Fig. S2, ESI). The $O^{2-} \rightarrow Ce^{3+}$ charge-transfer transition (at 256 nm) indicated the presence of oxygen vacancies.

After subtraction of reference CeZr spectrum (Fig. S2, ESI), all the solids showed an intense band (c.a. 425 nm) and weaker band (c.a. 700 nm), both corresponding to d-d bands from Ni^{2+}. The wavelength of the maximum increased as follows: NiCeZr-CS (443 nm) < NiCeZr-SC (449 nm) < NiCeZr-CA (451 nm) < NiCeZr-IM (498 nm). The upshift indicated weaker nickel-support interactions [38]. Accordingly, the one-pot methods produced solids with high Ni-surroundings interaction.

The band gap (Eg) for the bare CeZr was 3.1 eV, in concordance with literature [39]. Nickel inclusion in the CeZr lattice modified its band structure, as suggested by the decrease in Eg (Table 1). Interestingly, the sol-gel method seemed to favor such intimate contact.

3.3. Redox properties by H_2-TPR

The reduction profile of bulk NiO (Fig. 3) was composed by a broad peak at 355 °C, followed by a shoulder at 415 °C. The reduction profile of CeZr was composed by three contributions, indicating the presence of various oxygen species: (i) a small peak at low temperature (< 250 °C), ascribed to surface oxygen at the oxygen vacancies (O^V); (ii) intermediate temperature peak (362 °C), attributed to the $Ce^{4+} \rightarrow Ce^{3+}$ reduction in the surface; (iii) high temperature peak (514 °C), attributed to the $Ce^{4+} \rightarrow Ce^{3+}$ reduction in the bulk. The reducibility of the cerium oxides is related to the ability of cerium to reversibly change oxidation states between Ce^{4+} and Ce^{3+} [40]. The total H_2 uptake for bare CeZr (Table 2) exceeded by 13% the theoretical for Ce^{4+} to Ce^{3+} reduction, indicating the reduction of the oxygen at O^V.

The reduction profiles of NiCeZr solids were notably different from those bare CeZr and bulk NiO. In general, the reduction started at a

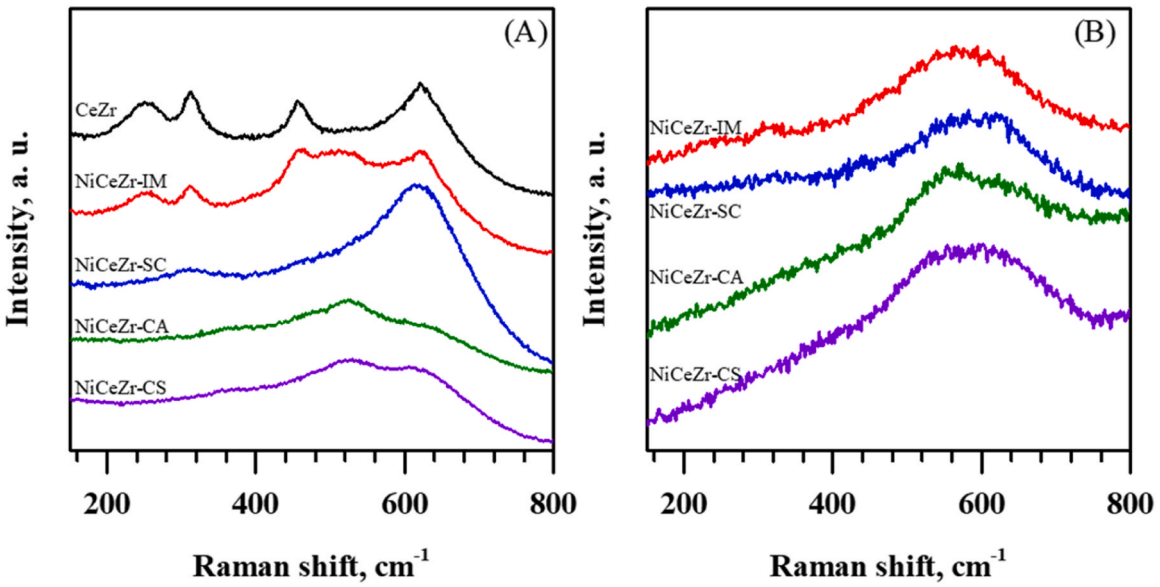

Fig. 2. Raman spectra for (A) calcined and (B) reduced forms of the materials.

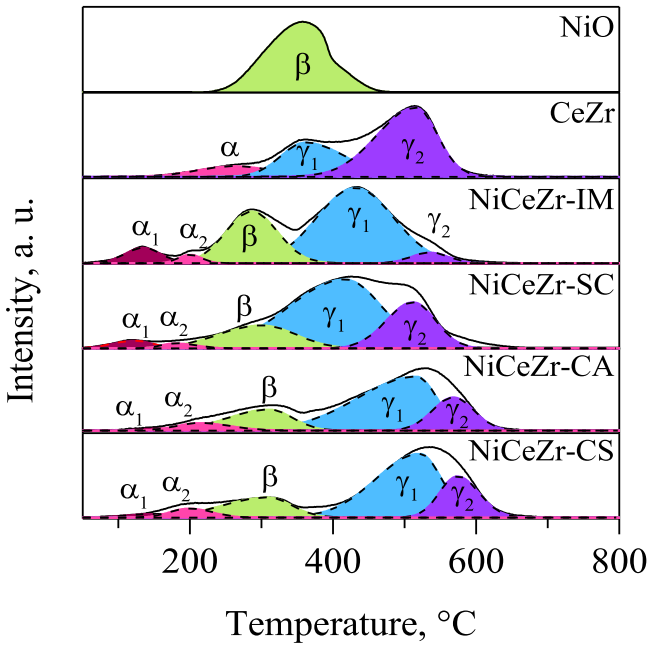

Fig. 3. Reduction profiles from NiCeZr and reference NiO and CeZr.

Table 2
Redox and surface characteristics of the materials.

Catalyst	Total H_2 uptake ($mmolH_2/g$)	Peak contributions (%)			Acid sites density ($(10^{17}\cdot sites/m^2)^c$	metal/ acid (sites/ sites)
		α	β	γ		
CeZr	0.65 (113%)	9.7	0.0	90.3	n.a.	0.0
NiCeZr-IM	2.15 (105%)	7.8	27.9	64.3	10.8	0.14
NiCeZr-SC	2.77 (125%)	3.6	12.7	83.7	10.2	0.22
NiCeZr-CA	2.18 (118%)	8.3	16.4	75.3	2.4	0.21
NiCeZr-CS	2.28 (109%)	7.6	14.5	77.9	3.0	0.34

lower temperature than bare CeZr, and resulted in a more complex profile. The peaks were classified into three main contributions, according to the species which was predominantly reduced: (i) α contribution (below 250 °C), ascribed to the easily reducible oxygen adsorbed at O^V sites; (ii) β contribution (in the range 250–320 °C), assigned to the reduction of NiO; (iii) γ contribution (320–700 °C range), attributed to the reduction of both Ni^{2+} in the solid solution and bulk Ce^{4+}.

α contribution consisted on two peaks: (i) α_1 peak, at lower temperature, associated to the reduction of oxygen ions at the O^V-NiO interface; and (ii) α_2 peak, linked to the reduction of oxygen ions formed on the CeZr surface after O^V was filled with H_2 [41]. In general, the ratio of intensities $\alpha_1/(\alpha_1+\alpha_2)$ was much lower for the solids prepared by coprecipitation, due to their outstanding S_{BET}. The absence of α1 in the bare CeZr was due to the absence of NiO.

Also, γ contribution could be deconvoluted into two peaks: (i) the low temperature peak (peak γ_1), attributed to the concomitant reduction of both Ni^{2+} in the solid solution (harder to reduce) [32], and surface Ce^{4+}; (ii) the high temperature peak γ_2, assigned to the reduction of bulk Ce^{4+}.

Similar to that for CeZr, for all the Ni-containing assays, the hydrogen uptake exceeded the theoretical for the reduction of all Ni and Ce species (assuming at the beginning of TPR they were as Ni^{2+} and Ce^{4+}), in agreement with others [32]. It was attributed to the hydrogen uptake in the reduction of oxygen adsorbed on O^V (α peaks). The hydrogen uptake for α peak ranged between 3.6% and 8.3% of the total consumption. Ni addition boosted the H_2 uptake from α peak (CeZr: 0.063 $mmol_{H2}/g$ vs. NiCeZr-CA: 0.181 $mmol_{H2}/g$).

NiCeZr-IM solid showed the highest and lowest hydrogen uptake due to β and γ peaks, respectively (Table 2), indicating it contained more Ni^{2+} as NiO and less as solid solution. Both materials prepared by coprecipitation presented wider β peaks, indicating several types of surface nickel coexist, i.e., NiO of varying sizes at the surface. The lack of symmetry of the γ peaks in all the one-pot prepared materials denoted the existence of multiple oxygen species in the solid Ni-Ce-Zr, such as Ce-O and Ni-O.

The remarkable downshift in the reduction temperature of the Ce^{4+} species for NiCeZr-IM and NiCeZr-SC materials when comparing with CeZr was due to the H_2 spillover onto Ni^0. This effect was less pronounced in both solids prepared by coprecipitation, suggesting stronger Ni-CeZr interaction that hindered the reduction of Ce^{4+}. In conclusion, the interaction with the CeZr solid solution influenced the reduction of Ni^{2+} species, and Ni^{2+} species also influenced (promoting) the reduction

of the Ce^{4+} in the solid solution through H_2 spillover.

3.4. Metal sites and morphological characterization

The catalysts showed variable amount of metal sites (1.06–1.95 $\times 10^{19}$ sites/g_{cat} range), and dispersions (2.4–5.0% range) (Table 2), which could be ascribed to the differences in the crystallite sizes and nickel loadings. The solids consisted on composite materials with a mixture of single NiO particles, and Ni^{2+} species strongly interacting with CeZr environment that, according to TPR, are reduced at different temperatures. Upon reduction of NiO, they could be agglomerated on the surface, giving rise to a big Ni^0 particles. Indeed, these crystallites were the ones visible by XRD. In contrast, the Ni^0 grown through the exsolution of Ni^{2+}, could give rise to smaller particles that could not be detected by XRD.

EDX maps (Fig. S3, ESI) shows that, irrespective of synthesis method, both Ce and Zr were uniformly distributed within the grains of the solid, indicating a homogeneous Ce-Zr phase, consistent with XRD. Both elements superimposed with O element, indicating they were oxidized. Although this was expected for Zr, due to its low reducibility, it was also observed for Ce, which could be due to the surface oxidation of Ce during the transfer of the samples to the analysis device.

Regarding Ni, all the solids presented zones with high and low concentration, suggesting non-uniform distribution of nickel. The bright areas consisted on agglomerates, consistent with the large nickel crystallites shown by XRD. This indicated that Ni aggregation occurred during the reduction treatment. The Ni dispersion depended on the synthesis method. NiCeZr-IM showed areas with very high agglomeration. However, NiCeZr-SC showed more homogeneous distribution, which could indicate good insertion of Ni^{2+} within the Ce-Zr structure. Both materials prepared by coprecipitation presented similar and quite homogeneous distribution of Ni, NiCeZr-CA presenting smaller spots than NiCeZr-CS.

3.5. Surface acidity

The NH_3-TPD profiles (Fig. S4, ESI) consisted on complex profile in the 90–800 ºC range, indicating the presence of acid sites with different strengths. The materials presented total acid sites density below than 11×10^{17} sites/m^2, suggesting low acid character of the solids, consistent with the low Ce/Zr ratio. The acid sites density for both solids prepared by coprecipitation was 3–4 times lower than for the others, which could be due to the presence of traces of Na. For all the solids, weak sites predominated, with around 70% (Table S2, ESI). The solids prepared by one-pot method, which promoted the intimacy in the NiCeZr solid, presented the highest contribution of strong sites. For the one-pot synthesized catalysts, both the surface enrichment in Zr and the higher concentration of surface oxygen (see XPS results) could contribute to the increased contribution of strong acidic centers [42]. In addition, acid sites are expected to be of Lewis-type [43].

For the hydrogenolysis of glycerol on bifunctional catalysts without exogenous H_2, the metal sites provide both dehydrogenation (C-H scission) and hydrogenation (C═O hidrogenation) function, while the acid sites provide the dehydration (C-O scission) function [6]. Therefore, the relative abundance between both type of sites and the proximity between them are key parameters for the product distribution [12]. As a rough indicator of this joint effect, we have calculated the ratio metal-to-acid sites (Table 2). For the NiCeZr series catalysts, the lowest metal-to-acid sites ratio (0.14, Table 2) corresponded to NiCeZr-IM catalyst, which increased to 0.21–0.34 for the one-pot synthesized catalysts.

In parenthesis, percentage of reduction with respect to the theoretical for the complete reduction of all nickel and cerium ions, assuming they are as Ni^{2+} and Ce^{4+}; n.a. not analysed.

3.6. Surface characterization by XPS

For all the calcined solids, signals from both Ce^{3+} and Ce^{4+} in the complex Ce 3d spectra are observed (Fig. S5, ESI), containing two doublets for Ce^{3+} (v′/u′, v_0/u_0) and three doublets for Ce^{4+} (v/u, v″/u″, v‴/u‴), corresponding to Ce $3d_{5/2}$ and Ce $3d_{3/2}$ peaks. The difference between these two signals (Table S3, ESI) ranged between 18.3 and 18.6 eV for all samples, in line with literature [44]. As expected, cerium was mainly as Ce^{4+} for the calcined solids (Table 3). The surface Ce^{3+} percentage decreased as follows: NiCeZr-IM (27.4) >> NiCeZr-CA (17.3) > NiCeZr-CS (16.4) > NiCeZr-SC (15.6).

Ni $2p_{3/2}$ core-level spectra contains $2p_{3/2}$ and $2p_{1/2}$ spin-orbit split doublets. For the sake of simplicity, the peak fitting was performed for the Ni $2p_{3/2}$ regions (Fig. 4A, Table S3, ESI). Independent of the solid, the signal was composed by a main peak (in the range 851–859 eV) and the satellite peak (at around 862 eV), both characteristics of Ni^{2+} species [45]. No other features were observed, indicating that all the calcined solids contained only Ni^{2+}. A blueshift (0.3–0.7 eV) in the main peak of the one-pot synthesized solids as compared to NiCeZr-IM, consistent with the presence of Ni^{2+} cations strongly interacting with the Ce-Zr surroundings [46]. The decrease in the satellite-to-main peak area (Table S2, Supplementary Material) for the one-pot synthesized solids supported the above idea [47]. All the observed results were consistent with XRD, DRS and H_2-TPR results.

The O1s XPS spectra could be deconvoluted in three peaks (Fig. S6A, ESI): (i) peak at c.a. 529.5 eV, assigned to the surface lattice oxygen (O^L); peak at 531.0 eV, attributed to adsorbed oxygen species (O^V); and peak at 533 eV (O^C) due to surface chemisorbed species, such as water or carbonate species [48]. In ceria-containing solids, the surface oxygen vacancies (O^V) are associated to the presence of Ce^{3+} ions [49]. A linear correlation was found (Fig. S7, ESI) between the content of Ce^{3+} and the fraction of surface oxygen vacancies (O^V/O^L). Consequently, NiCeZr-IM catalyst prepared by surface addition of nickel, showed the highest concentration of surface oxygen vacancies, involving easier reducibility of Ce^{4+} (peak α + β in H_2-TPR). The less intimate and weaker interaction of the Ce^{4+} in the lattice with Ni^{2+} species reinforced the above conclusion.

All the calcined solids showed very similar Zr 3d core-level spectra, which consisted on $3d_{5/2}$ and Zr $3d_{3/2}$ peaks, at around 183.0 eV and 185.7 eV, respectively, with constant ΔBE of 2.74 eV, both characteristics attributable to Zr^{4+} species (Fig. S8 and Table S3, ESI). Moreover, the binding energies of Zr 3d of our NiCeZr solids were higher than those in bare ZrO_2 from literature [50], indicating that Zr strongly interacted with its surroundings, acting as an electron donor. Finally, XPS analysis indicated that both solids synthesized by coprecipitation contained in their surface traces of Na (2.2–2.8 atom%).

Upon reduction, the XPS spectra of all elements notably changed. In the Ce 3d spectra (Fig. S5B, ESI), only consisted on signals from Ce^{3+}, indicating the reduction of all Ce^{4+} ions to Ce^{3+}, consistent with H_2-TPR. The Ni 2p XPS spectra for all the reduced solids (Fig. 6B) were composed by two peaks at c.a. 857 and 852.5 eV, which were attributed to Ni^{2+} and Ni^0 species, respectively. In addition, it was found a weak satellite peak (at c.a. 860 eV), which was consistent with the presence of Ni^{2+}

Table 3
Surface chemical composition from XPS (atom).

Catalyst	Zr/Ce	Ni/(Ce+Zr)	Ce^{3+}/(Ce^{4+}+Ce^{3+})	O/(Zr+Ce+Ni)	Ni^0/Ni_{total}
NiCeZr-IM	3.6 (4.1)	1.37 (0.79)	0.27 (1.0)	1.46 (0.49)	(0.60)
NiCeZr-SC	7.6 (5.6)	0.18 (0.08)	0.16 (1.0)	2.00 (0.61)	(0.71)
NiCeZr-CA	8.0 (5.6)	0.23 (0.12)	0.17 (1.0)	1.83 (0.70)	(0.74)
NiCeZr-CS	7.6 (5.8)	0.17 (0.08)	0.16 (1.0)	1.89 (0.70)	(0.70)

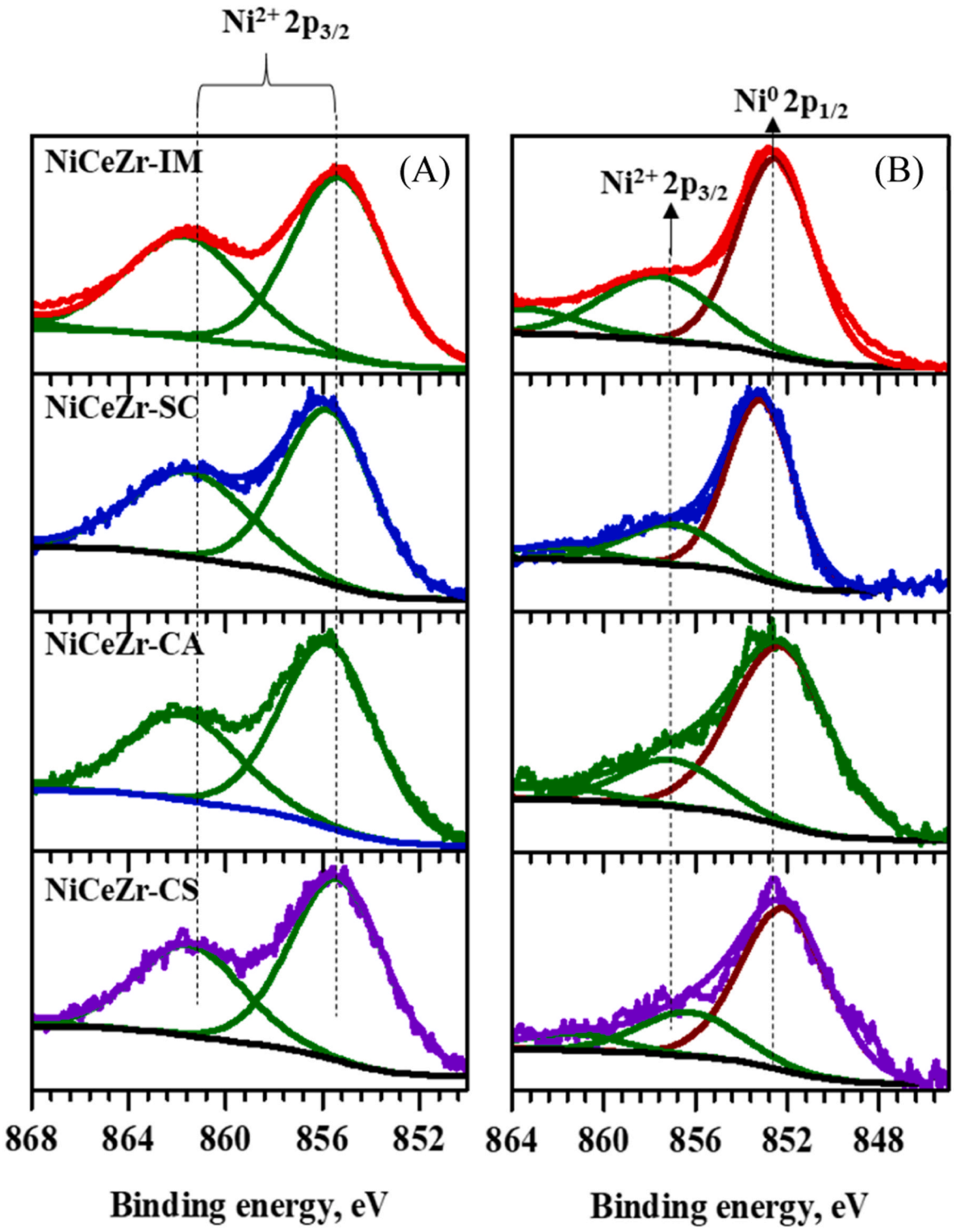

Fig. 4. Detailed Ni 2p spectra for calcined (A) and reduced (B) solids.

species [51] The intensity of the Ni^0 peak was notably higher than that of Ni^{2+}, indicating that most of the surface nickel was reduced (Table 3). In the case of NiCeZr-IM solid, 60% of the surface nickel was reduced, and it increased to 70–74% for the one-pot synthesized catalysts. This could be due to the smaller NiO particles in the surface of the solids prepared by one-pot. The O 1 s spectra (Fig. S6B, ESI) showed a downshift in the O binding energy upon reduction (by 0.2–0.4 eV), which could be attributed to the polarization of the O-Metal bonds [52].

The area under the different deconvoluted peaks was used to quantify the fraction of each Ni, Ce and O species on the catalyst surface (Table 3). In the calcined forms of the solids, and compared to bulk composition, the surface of NiCeZr-IM enriched in Ce. On the contrary, the surface of all the one-pot synthesized solids enriched in Zr (Zr/Ce: 5.67 for bulk vs 7.6–8.0), in agreement with literature [53]. Upon reduction, the ratio Zr/Ce in the surface decreased (enriched in Ce) with respect to the calcined forms, except for the solid prepared by impregnation.

The highest (Ni/Ce+Zr) ratio was for NiCeZr-IM (1.37 vs 0.17–0.23

for the one-pot solids), consistent with the XRD and H_2-TPR results. Compared to bulk composition, (where Ni/(Ce+Zr) atom ratios ranged between 0.188 and 0.247), NiCeZr-IM notable enriched in Ni, consistent in the Ni addition method. In the case of NiCeZr-CA solid, which had the lowest Ni loading (Table 1), its surface also was enriched in Ni (Ni/(Ce+Zr): 0.188 vs 0.23 in the bulk and surface, respectively), which is consistent with the presence of highly dispersed NiO, invisible for XRD. In this regard, a linear correlation between the β peak (associated with NiO reduction in the H_2-TPR) and the surface Ni content (determined by XPS) could be deduced for the one-pot synthesized solids (Fig. S9, ESI). However, NiCeZr-IM assay fell out of the trend, with boosted Ni fraction on the surface.

In parenthesis, values for reduced solids (10% H_2/He, 600 ºC, 1 h).

Unexpectedly, upon reduction, Ni/(Ce+Zr) ratio decreased by half for all the catalysts, likely due to the decoration of Ni particles by ceria [54]. This fact could explain both the decrease in Ni concentration and increase in Ce (lower Zr/Ce), specifically for one-pot synthesized solids. As expected, O/(Zr+Ce+Ni) surface ratio tri-fold decreased for reduced solids, indicating O removal by reacting with hydrogen.

4. Catalytic test

Blank test with bare CeZr showed very low glycerol conversion (3%) with almost null gas production. NiCeZr-CS with no reduction treatment achieved 9% glycerol conversion. In these conditions, the surface acidity of the catalyst was responsible of the glycerol conversion, since hydroxyacetone was the only liquid product detected, with negligible gas production [55]. Both results pointed that hydrogen production and glycerol hydrogenolysis might be attributed to metallic nickel. Similar outcomes was reported by others for methanol APR [20,56].

There were notable differences in the glycerol conversion among the catalysts (Fig. 5). While NiCeZr-IM showed 6.3% glycerol conversion, the insertion of Ni into the CeZr lattice (catalysts synthesized by one-pot methods) had a positive effect on glycerol conversion, which reached the highest conversion (75.3%) for the NiCeZr-CS catalyst. Among catalysts families, activity increased as follows: impregnation < sol-gel < coprecipitation. These results suggested that the surface acidity was detrimental for the glycerol conversion, while possessing high S_{BET} was beneficial. In the case of NiCeZr-CS catalyst, its highest metal sites density (Table 1) could also contribute to its outstanding activity.

Same trend was observed for the carbon yield to liquid, which passed from 2.4% for catalyst NiCeZr-IM to 56.3% for catalyst NiCeZr-CS. On the other hand, the maximum carbon yield to gases (25%) was achieved by NiCeZr-CA catalyst.

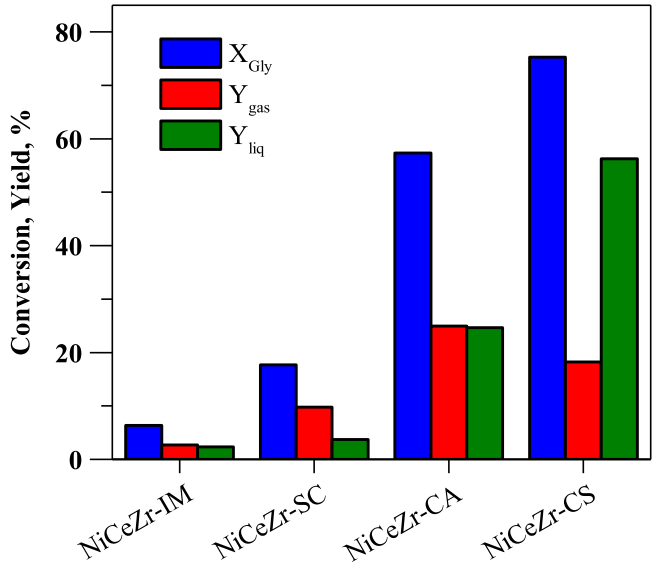

Fig. 5. Effect of the catalyst synthesis method on glycerol hydrogenolysis. Reaction conditions: T = 235 ºC, P = 35 bar, WHSV= 12 h^{-1}, feed composition = 10 wt% gly/water, data at 3 h TOS.

4.1. Gas products

Table 4 summarizes the gas phase products analysis. The gas product was mainly composed by H_2, CO_2, CO, CH_4 and C_{2+} alkanes (which included ethane and propane), the major compound depending on the catalyst preparation method. For NiCeZr-IM and NiCeZr-SC, the major compound in the gas phase was H_2; however, for catalysts prepared by coprecipitation, the major compound was CO_2. Interestingly, the H_2 concentration in the gas product followed an opposite trend with glycerol conversion, indicating that the most active catalysts contributed to hydrogen-consuming side reactions, such as hydrogenation of dehydrated intermediates and CO/CO_2 hydrogenation. Ideally, the glycerol APR gives $H_2/CO_2 = 7/3$ ratio. Among our catalysts, NiCeZr-IM and NiCeZr-SC approached this value, while for the other one-pot synthesized catalysts, the ratio decreased to a c.a. 0.45 for both catalysts prepared by coprecipitation. These results were consistent with the hydrogen consumption for the hydrogenolysis of glycerol and the subsequent liquid intermediates. Moreover, the increase in $Y_{liquids}$ for these catalysts (Fig. 5) supported the above conclusion.

Methane was also obtained for all the catalysts, in the 19.3–26.6% range. This was not unexpected, since Ni is active for CH_4 production from CO/CO_2 hydrogenation, due to its ability to form subcarbonyl species [57]. The ratio $CH_4/(CO+CO_2)$ was chosen to evaluate the methanation ability of our catalysts. The catalyst prepared by impregnation showed the highest ratio (2.07), which decreased to 0.85–0.36 for the one-pot synthesized catalysts. Accordingly, it could be deduced that catalysts prepared by Ni solution into the CeZr lattice were less efficient for CO/CO_2 hydrogenation. The lower concentration of Ni in the surface [58] and lower concentration of oxygen vacancies (O^V) [59] of these catalysts could explain this behavior. The selectivity to alkanes (computing $CH_4 + C_{2+}$) markedly decreased for the one-pot synthesized catalysts (from 3.85 for NiCeZr-IM to 2.1–0.49% for the one-pot), in good correlation with the surface acidity. Similar outcome was found for others in the APR reaction [60].

No CO was detected in the gas product for catalyst NiCeZr-IM, indicative of its effectiveness for the WGS reaction; however, for the one-pot synthesized catalysts, the gas contained 1.1–4.6% CO, suggesting that, over these catalysts, the WGS reaction was suppressed. Apart of by WGS, CO also could be converted by methanation. In Ce-containing catalysts, the high WGS activity is correlated with the amount of oxygen vacancies [61]. As well, WGS activity has been correlated with surface basicity of catalysts [62]. In the case of NiCeZr-IM catalysts, its highest amount of oxygen vacancies (O^V, Fig. S7) related to its higher surface Ce^{3+} percentage, could explain its outstanding WGS activity, facilitating the activation of the water molecule. In addition, the very little contribution of strong acid sites (7%, Table S2 ESI) in this catalyst did not affect its WGS activity.

Part of the carbon fed as glycerol was obtained in the form of liquid products. According to the literature [63], the liquid-phase

Table 4
Composition of the gas product, at 3 h TOS.

Catalyst	H_2 (%)	CH_4 (%)	CO (%)	CO_2 (%)	C_{2+} (%)	H_2/CO_2	Y_{H2} (%)	Y_{CH4} (%)
NiCeZr-IM	49.7	26.6	0.0	12.8	10.9	3.87	1.0	2.2
NiCeZr-SC	41.3	20.1	9.3	14.3	15.0	2.88	2.3	2.6
NiCeZr-CA	20.7	23.6	1.1	47.8	6.7	0.43	2.4	6.2
NiCeZr-CS	24.3	19.3	2.9	50.2	3.3	0.48	2.3	4.3

hydrogenolysis of glycerol on bifunctional catalysts comprises three main paths consisting on dehydration/dehydrogenation/hydrogenation reactions [64]. Path A consists on the sequential dehydrogenation/decarbonylation (C-C scission) on metal sites that produces CO and ethylene glycol (EG). This reaction pathway could be simultaneously accomplished through the conversion of EG, for example into ethanol, by dehydration/hydrogenation of ethylene glycol [65]. Path B comprises the dehydration on acid sites of terminal hydroxyl to hydroxyacetone (HA), product of primary hydroxyl group dehydration (C-O scission), and subsequent hydrogenation, on metal sites, to 1,2-propylene glycol (PG). Further dehydration/hydrogenation steps can produce mono-alcohols (1-propanol and 2-propanol). Finally, Path C starts with dehydration of the secondary hydroxyl to 3-hydroxypropanal, whose hydrogenation leads to 1,3-PG. Path B is preferred for Lewis acid sites while Brönsted acid sites are more prone to give Path C [66]. Secondary C-C breaking reactions are responsible for the formation of C2 and C1 products.

4.2. Liquid products

In the aqueous-phase transformation of glycerol over NiCeZr catalysts series, the distribution of liquid products depends on the method of preparation (Table 5). The main liquid products were HA, PG, EG and ethanol, which account for above 94% of all detected products. Other compounds (methanol, 1-propanol and acetone) accounted for below 7%. The absence of Path C products was consistent with the Lewis acidic nature of the CeZr-based catalysts [43].

The highest selectivity to PG was achieved by both catalyst prepared by coprecipitation, with the highest selectivity of 50% for NiCeZr-CS. On the contrary, these two catalysts showed the lowest selectivity to HA. According to the reaction scheme described above, dehydration of the glycerol produces HA, which, by successive hydrogenation of the C═O bond, produces PG. The distribution between these two products from Path B indicated that the metal sites on the both catalysts prepared by coprecipitation had higher hydrogenation capacity, being the lowest for NiCeZr-IM assay. This result was attributed to the high metal-to-acid sites ratio (Table 2) for the catalysts prepared by coprecipitation, which could enhance the hydrogenation of HA, leading to the higher selectivity towards PG. Despite having a metal-to-acid sites ratio similar to NiCeZr-CA, the product distribution of NiCeZr-SC catalysts pointed to low hydrogenation capacity, which could be due the bigger Ni^0 crystallites that lowered intimacy between both kinds of sites. It was worth to note that the highest selectivity to acetone was achieved by both catalysts prepared by coprecipitation, consistent with their higher selectivity to PG, precursor of acetone.

As a general trend, a trade-off between EG and ethanol (both products from Path A) could be drawn. As ethanol is a product of the succesive dehydration and hydrogenation of EG, it confirmed that the metal sites of the catalysts synthesized by coprecipitation were more active for hydrogenation. The products identified might be considered under bifunctional characteristics of the catalysts, where both the acid sites and metallic sites could contribute to the conversion of substrate [67].

Considering the selectivity of the liquid products, products from path B (especially HA and PG) prevailed, consistent with the occurrence of hydrogenolysis.

For all the investigated catalysts, primary products dominated over secondary products (Table 5) with selectivity towards primary products above 75%. Interestingly, both catalysts prepared by coprecipitation exhibited the highest selectivity towards secondary products (16.6–26.9% range). These indicated that these catalysts, compared to NiCeZr-IM, promoted additional C-C or C-O bond scission. These results were consistent with the high metal-to-acid sites ratio with high intimacy of catalysts prepared by coprecipitation [68]. Moreover, the selectivity analysis based on C–C and C–O bond scissions revealed that the highest selectivity was for the C–O bond scission, exceeding 60% (Table 5). Again, the catalysts prepared by coprecipitation were the most selective for C–O scission, indicating that the presence of both nickel and acid sites synergistically enhanced the hydrogenation capacity and favored the cleavage of C–O bonds [69]. The competitive C–C and C–O bond cleavages were strongly affected by the metal-to-acid sites ratio [70]. Overall, the liquid product contained less oxygen than the feedstock (lower O/C), being the catalysts with higher selectivity to C–O scission those with the higher hydrodeoxygenation capacity.

5. Characterization of spent catalysts

The challenges on the design of a catalyst for the aqueous-phase biomass treatment applications are diverse, as deactivation caused by metal leaching, phase transformations, or metal sinterization, among others [71]. In order to investigate the changes undergone by catalysts, the spent catalysts were analyzed. The N_2 isotherms of the post-reaction catalysts were similar than those of their reduced counterparts (Fig. S10, ESI). S_{BET} of the spent catalysts did not varied with respect to their reduced counterparts, except for both prepared by co-precipitation, which slightly increased the surface area. These results contrasted with others [72], which observed rapid decrease in the S_{BET} for non-doped ZrO_2-based materials under hydrothermal conditions. Therefore, it could be concluded that doping with Ce could increase its hydrothermal resistance [73]. Both catalysts derived from co-precipitation were the only which appreciable modified their PSD curves. In the case of spent NiCeZr-CA catalyst, the contribution of the biggest pores decreased, reaching a PSD similar to its calcined precursor. In the case of spent NiCeZr-CS catalyst, the PSD became wider, suggesting generation of new pores.

The XRD profiles of the spent catalysts (Fig. 6A) showed differences with respect those of the reduced forms, such as the weakening of the Ni^0 intensity, and the development of peaks from NiO, the latter suggesting that part of the nickel was oxidized. In other studies with nickel aluminate-derived catalysts oxidation of surface caps of nickel was also reported [74]. The main XRD feature, corresponding to ceria-zirconia solid solution, remained unvaried with respect to those for reduced counterparts, suggesting no phase-variation. No other crystalline phases such as carbonates or graphitic carbon were identified. Over Ce-containing catalysts, formation of cerium hydroxycarbonates ($CeOHCO_3$) was reported under APR [20]. The absence of XRD peaks from such carbonate phase could be due to the low Ce/Zr ratio of our catalysts. Formation of coke is usually reported as a deactivation cause for APR catalysts [75]. The absence of XRD peak for coke for our catalysts could be due to its low content (see Raman results) and low graphitization.

Table 5
Selectivities to liquid products.

Catalyst	EG	Ethanol	HA	PG	Methanol	1-propanol	Acetone	Primary products	Secondary products	C-C	C-O	O/C
NiCeZr-IM	36.2	0.0	63.8	0.0	0.0	0.0	0.0	100	0.0	36.2	63.8	0.76
NiCeZr-SC	38.8	2.6	56.8	0.0	0.6	1.2	0.0	95.6	4.4	39.4	60.6	0.76
NiCeZr-CA	7.1	11.7	29.2	47.1	1.1	0.7	3.1	83.4	16.6	8.2	91.8	0.66
NiCeZr-CS	5.4	19.7	18.7	50.0	1.6	1.0	4.6	74.1	26.9	7.0	94	0.64

Primary products: single C–O or C–C bond scission (EG, PG, HA)
Secondary products: more than a single C–O or C–C bond sccision (ehanol, methanol, acetone, 1-propanol)

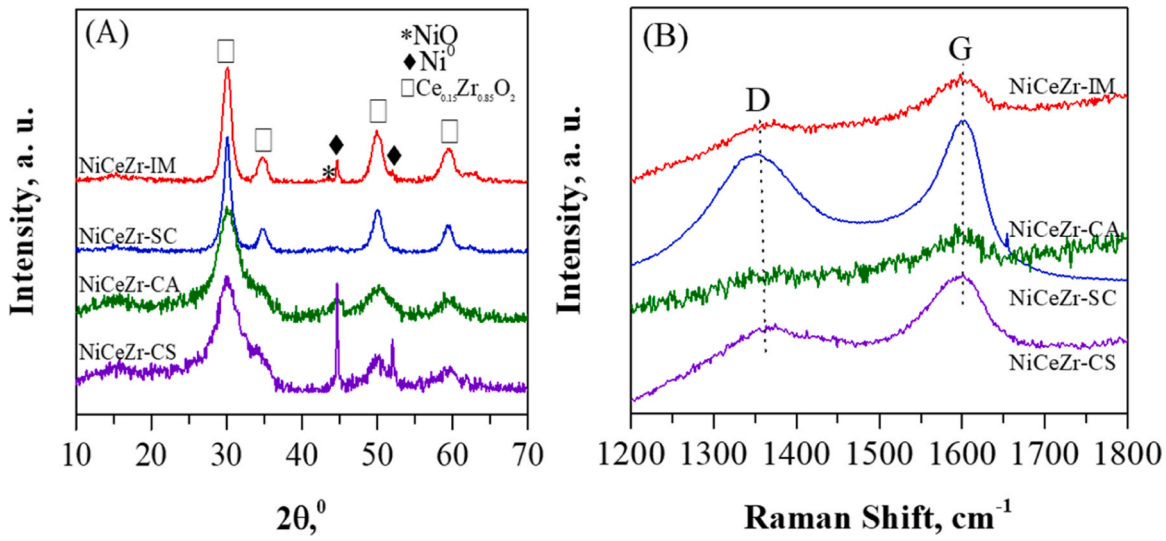

Fig. 6. XRD patterns (A) and Raman spectra (B) of spent catalysts.

As a general trend, the size of Ni^0 crystallite notably decreased for the spent catalysts (Table 6). The most notable decrease in size was for NiCeZr-SC and NiCeZr-CA (decrease by 76–87%). NiCeZr-CS catalyst deviated from this trend, since Ni^0 size passed from 46 to 55.8 nm after usage, indicating a coalescence of Ni^0 crystallites. The variation in NiCeZr crystallite size was consistent with the variation in S_{BET} of the spent catalysts.

In the Raman spectra of the post-reaction catalysts (Fig. 6B), both the D and G bands were observed. These bands were associated to carbonaceous structures [76], which indicated that carbonaceous deposits were generated during reaction, despite invisible for XRD. Specifically, D band (at ~ 1350 cm^{-1}) was associated to amorphous carbonaceous structures, while the G band (at ~ 1600 cm^{-1}) was attributed to graphitic carbon. The low intensity of both bands indicated low amount of carbonaceous deposits. The oxygen mobility related to the oxygen vacancies of CeZr could contribute to the low carbon deposition [77]. The ratio between the intensities of the D and G bands (I_D/I_G, Table 6) ranged in the interval 0.83–0.86, indicating low degree of graphitization. These results were in agreement with the absence of XRD peaks from graphitic carbon.

Leaching of the active phase could irreversibly deactivate the catalyst. At a first glance, Ni underwent greatest leaching among all metals, with negligible leaching for Ce, while Zr did not leached. Spent NiCeZr-CS catalyst showed the highest loss of nickel (twice of those for the other catalysts). The joint effect of its big Ni^0 particles and its high surface area (more exposed to be attacked by water) could contribute to its higher Ni (and Ce) leaching. In aqueous medium, the mechanism of transition metal leaching consisted on the oxidation of the metal and subsequent dissolution as hydroxyl. The acidity of the reaction medium [78] and the chelation [79] could contribute to nickel leaching. The detection of XRD peaks from NiO in the spent catalysts was consistent with the relatively high degree of leaching.

6. Conclusions

In this work, a series of NiCeZr catalysts were prepared, characterized, and tested in the aqueous-phase transformation of glycerol. The effects on the reaction performance of embedding nickel during the synthesis of catalysts was investigated. The one-pot synthesis of NiCeZr solids led to hetero-structure systems with NiO and NiCeZr solid solutions. Results revealed differences among catalysts textural properties, which significantly affected their activity in glycerol conversion. The structural characterization confirmed the successful integration of Ni into the CeZr lattice, especially for the catalysts synthesized using one-pot methods.

Ni addition generated oxygen vacancies, especially for the catalyst prepared by impregnation. The one-pot synthesized solids showed stronger Ni-CeZr interaction than that prepared by impregnation, which affect the reducibility. When Ni was embedded in the CeZr oxide, upon reduction, resulted in less acid than that prepared by impregnation, and increased the metal-to-acid ratio.

Surface acidity and more specifically, the metal-to-acid sites density ratio was found to have a profound impact on glycerol conversion. High metal-to-acid sites density ratio resulted in high glycerol conversion rates, highlighting the importance of maintaining a delicate balance between acid and metal sites. NiCeZr-CS was the most active catalyst, with 75.3% conversion. Both catalysts prepared by coprecipitation demonstrated high hydrogenation efficiency, which was attributed to their high metal-to-acid sites ratio and the intimate interaction between these sites. Both catalysts selectively produced 1,2-propylene glycol.

This study revealed that the NiCeZr series catalysts exhibited notable stability under hydrothermal conditions, despite challenges like metal leaching and phase transformations. However, the catalyst preparation methods could influence the extent of nickel lixiviation and oxidation, and the carbonaceous deposit formation, underscoring the need for further stabilization.

Table 6
Textural properties and leaching concentration of NiCeZr-X used samples.

Catalyst	S_{BET} (m^2/g)	V_{pore} (cm^3/g)	d_{pore} (nm)	d_{NiCeZr} (nm)	d_{Ni^0} (nm)	I_D/I_G	Metals leached (wt%)	
							Ni	Ce
NiCeZr-IM	81.7 (0.0%)	0.124 (−8.1%)	4.5 (−13.5%)	5.9 (+9.3%)	26.3 (−44%)	0.83	2.4	0.03
NiCeZr-SC	54.8 (+0.2%)	0.063 (+21.1%)	3.9 (+11.4%)	6.2 (+3.3%)	14.7 (−76%)	0.85	2.0	0.13
NiCeZr-CA	238.4 (+7.8%)	0.255 (−5.9%)	3.7 (−5.1%)	2.5 (−3.8%)	6.5 (−78%)	0.86	2.1	0.15
NiCeZr-CS	217.7 (+14.8%)	0.306 (+21.9)	4.5 (+7.1%)	3.3 (−15.4%)	55.8 (+21%)	0.83	4.7	0.90

In parenthesis, percentage variation respect freshly reduced forms. n. d.: not detected

CRediT authorship contribution statement

N.V.H: Investigation, Writing – original draft, Data curation. **U.I.V:** Formal analysis, Writing – review & editing. **J.L.A:** Funding acquisition, Conceptualization, Writing – review & editing, Data curation. **M.A.G.O:** Resources, Funding acquisition, Supervision.

Declaration of Competing Interest

The authors declare that they have no known competing financial interests or personal relationships that could have appeared to influence the work reported in this paper.

Data Availability

Data will be made available on request.

Acknowledgments

This research was supported by grant PID2019-106692RB-I00 funded by MCIN/AEI/10.13039/501100011033. N.V.H. would like to thank MICINN for the pre-doctoral grant (BES-2017-081580). Likewise, the authors thank for technical support provided by SGIker of UPV/EHU and European funding (ERDF and ESF).

Author Agreement Statement

We the undersigned declare that this manuscript is original, has not been published before and is not currently being considered for publication elsewhere. We confirm that the manuscript has been read and approved by all named authors and that there are no other persons who satisfied the criteria for authorship but are not listed. We further confirm that the order of authors listed in the manuscript has been approved by all of us. We understand that the Corresponding Author is the sole contact for the Editorial process. He is responsible for communicating with the other authors about progress, submissions of revisions and final approval of proofs.

Appendix A. Supporting information

Supplementary data associated with this article can be found in the online version at doi:10.1016/j.jece.2023.111072.

References

[1] T.M.I. Mahlia, Z.A.H.S. Syazmi, M. Mofijur, A.E.P. Abas, M.R. Bilad, H.C. Ong, A. S. Silitonga, Patent landscape review on biodiesel production: Technology updates, Renew. Sustain Energy Rev. 118 (2020), 109526, https://doi.org/10.1016/j.rser.2019.109526.

[2] J. Kaur, A.K. Sarma, M.K. Jha, P. Gera, Valorisation of crude glycerol to value-added products: perspectives of process technology, economics and environmental issues, Biotechnol. Rep. 27 (2020), e00487, https://doi.org/10.1016/j.btre.2020.e00487.

[3] S. Zhu, X. Gao, Y. Zhu, Y. Li, Y. Li, Tailored mesoporous copper/ceria catalysts for the selective hydrogenolysis of biomass-derived glycerol and sugar alcohols, Green Chem. 18 (2016) 782–791, https://doi.org/10.1039/C5GC01766A.

[4] A. Syuhada, M. Ameen, M.T. Azizan, A. Aqsha, M.H.M. Yusoff, A. Ramli, M. S. Alnarabiji, F. Sher, In-situ hydrogenolysis of glycerol using hydrogen produced via aqueous phase reforming of glycerol over sonochemically synthesized nickel-based nano-catalyst, Mol. Catal. 514 (2021), 111860, https://doi.org/10.1016/j.mcat.2021.111860.

[5] F. Cai, D. Pan, J.J. Ibrahim, J. Zhang, G. Xiao, Hydrogenolysis of glycerol over supported bimetallic Ni/Cu catalysts with and without external hydrogen addition in a fixed-bed flow reactor, Appl. Catal. A-Gen. 564 (2018) 172–182, https://doi.org/10.1016/j.apcata.2018.07.029.

[6] A. Fasolini, D. Cespi, T. Tabanelli, R. Cucciniello, F. Cavani, Hydrogen from renewables: a case study of glycerol reforming, Catal 9 (2019) 722, https://doi.org/10.3390/catal9090722.

[7] W. Zhou, Y. Zhao, S. Wang, X. Ma, The effect of metal properties on the reaction routes of glycerol hydrogenolysis over platinum and ruthenium catalysts, Catal. Today 298 (2017) 2–8, https://doi.org/10.1016/j.cattod.2017.07.021.

[8] A.J. Reynoso, J.L. Ayastuy, U. Iriarte-Velasco, M.A. Gutiérrez-Ortiz, Cobalt aluminate spinel-derived catalysts for glycerol aqueous phase reforming, Appl. Catal. B: Environ. 239 (2018) 86–101, https://doi.org/10.1016/j.apcatb.2018.08.001.

[9] V.L. Yfanti, E.S. Vasiliadou, A.A. Lemonidou, Glycerol hydro-deoxygenation aided by in situ H_2 generation via methanol aqueous phase reforming over a Cu-ZnO-Al_2O_3 catalyst, Catal. Sci. Technol. 6 (2016) 5415–5426, https://doi.org/10.1039/C6CY00132G.

[10] R. Raso, L. García, J. Ruiz, M. Oliva, J. Arauzo, Aqueous phase hydrogenolysis of glycerol over Ni/Al-Fe catalysts without external hydrogen addition, Appl. Catal. B: Environ. 283 (2021), 119598, https://doi.org/10.1016/j.apcatb.2020.119598.

[11] M.L. Barbelli, F. Pompeo, G.F. Santori, N.N. Nichio, Pt catalyst supported on α-Al_2O_3 modified with CeO_2 and ZrO_2 for aqueous-phase-reforming of glycerol, Catal. Today 213 (2013) 58–64, https://doi.org/10.1016/j.cattod.2013.02.023.

[12] J. Harmel, L.I. Van Der Wal, J. Zečević, P.E. De Jongh, K.P. De Jong, Influence of intimacy for metal-mesoporous solid acids catalysts for: N-alkanes hydroconversion, Catal. Sci. Technol. 10 (2020) 2111–2119, https://doi.org/10.1039/C9CY02510C.

[13] A. Morales-Marín, J.L. Ayastuy, U. Iriarte-Velasco, M.A. Gutiérrez-Ortiz, Nickel aluminate spinel-derived catalysts for the aqueous phase reforming of glycerol: Effect of reduction temperature, Appl. Catal. B: Environ. 244 (2019) 931–945, https://doi.org/10.1016/j.apcatb.2018.12.020.

[14] R. Raso, A. Lete, L. García, J. Ruiz, M. Oliva, J. Arauzo, Aqueous phase hydrogenolysis of glycerol with in situ generated hydrogen over Ni/Al_3Fe_1 catalyst: effect of the calcination temperature, RSC Adv. 13 (2023) 5483–5495, https://doi.org/10.1039/D2RA07929A.

[15] T. Van Haasterecht, C.C.I. Ludding, K.P. De Jong, J.H. Bitter, Stability and activity of carbon nanofiber-supported catalysts in the aqueous phase reforming of ethylene glycol, J. Energy Chem. 22 (2013) 257–269, https://doi.org/10.1016/S2095-4956(13)60032-7.

[16] R.L. Manfro, A.F. da Costa, N.F.P. Ribeiro, M.M.V.M. Souza, Hydrogen production by aqueous-phase reforming of glycerol over nickel catalysts supported on CeO_2, Fuel Process. Technol. 92 (2011) 330–335, https://doi.org/10.1016/j.fuproc.2010.09.024.

[17] M.M. Rahman, T.L. Church, A.I. Minett, A.T. Harris, Effect of CeO_2 addition to Al_2O_3 supports for Pt catalysts on the aqueous-phase reforming of glycerol, ChemSusChem 6 (2013) 1006–1013, https://doi.org/10.1002/cssc.201200797.

[18] S. Jeon, Y.M. Park, K. Saravanan, G.Y. Han, B. Kim, J. Lee, J.W. Bae, Aqueous phase reforming of ethylene glycol over bimetallic platinum-cobalt on ceria-zirconia mixed oxide, Int. J. Hydrog. Energy 42 (2017) 9892–9902, https://doi.org/10.1016/j.ijhydene.2017.01.221.

[19] P. Biswas, D. Kunzru, Steam reforming of ethanol for production of hydrogen over Ni/CeO_2-ZrO_2 catalyst: Effect of support and metal loading, Int. J. Hydrog. Energy 32 (2007) 969–980, https://doi.org/10.1016/j.cattod.2017.08.030.

[20] M. Stekrova, A. Rinta-Paavola, R. Karinen, Hydrogen production via aqueous-phase reforming of methanol over nickel modified Ce, Zr and La oxide supports, Catal. Today 304 (2018) 143–152, https://doi.org/10.1016/j.cattod.2017.08.030.

[21] M.L. Barbelli, M.D. Mizrahi, F. Pompeo, G.F. Santori, N.N. Nichio, J.M. Ramallo-Lopez, EXAFS characterization of PtNi bimetallic catalyst, applied to glycerol liquid-phase conversion, J. Phys. Chem. C 118 (2014) 23645–23653, https://doi.org/10.1021/jp412512x.

[22] F. Bastan, M. Kazemeini, A.S. Larimi, Aqueous-phase reforming of glycerol for production of alkanes over Ni/$Ce_xZr_{1-x}O_2$ nano-catalyst: Effects of the support's composition, Renew. Energy 108 (2017) 417–424, https://doi.org/10.1016/j.renene.2017.02.076.

[23] G. Pipitone, G. Zoppi, R. Pirone, S. Bensaid, A critical review on catalyst design for aqueous phase reforming, Int. J. Hydrog. Energy 47 (2022) 151–180, https://doi.org/10.1016/j.ijhydene.2021.09.206.

[24] I.C. Sophiana, F. Iskandar, H. Devianto, N. Nishiyama, Y.W. Budhi, Coke-resistant Ni/$CeZrO_2$ catalysts for dry reforming of methane to produce hydrogen-rich syngas, Nanomater 12 (2022) 1556, https://doi.org/10.3390/nano12091556.

[25] Y. Zhao, L. Qi, Z. Cheng, Z. Zhou, Syngas production via combined steam and carbon dioxide reforming of methane over Ni-$Ce_xM_{1-x}O_2$ (M = Ti or Zr) catalysts, Ind. Eng. Chem. Res. 61 (2022) 12978–12988, https://doi.org/10.1021/acs.iecr.2c01915.

[26] K. Jeon, H. Na, Y. Lee, S. Ahn, K. Kim, J. Shim, W.J. Jang, D.W. Jeong, I.W. Nah, H. S. Roh, Catalytic deoxygenation of oleic acid over a Ni-$CeZrO_2$ catalyst, Fuel 258 (2019), 116179, https://doi.org/10.1016/j.fuel.2019.116179.

[27] O. Thoda, G. Xanthopoulou, G. Vekinis, A. Chroneos, Review of recent studies on solution combustion synthesis of nanostructured catalysts, Adv. Eng. Mater. 20 (2018), 1800047, https://doi.org/10.1002/adem.201800047.

[28] A. Martínez-Arias, M. Fernández-García, V. Ballesteros, L.N. Salamanca, J. C. Conesa, C. Otero, J. Soria, Characterization of high surface area Zr-Ce (1:1) mixed oxide prepared by a microemulsion method, Langmuir 15 (1999) 4796–4802, https://doi.org/10.1021/la981537h.

[29] R.R. Poolakkandy, M.M. Menamparambath, Soft-template-assisted synthesis: a promising approach for the fabrication of transition metal oxides, Nanoscale Adv. 2 (2020) 515–545, https://doi.org/10.1039/D0NA00599A.

[30] Z. Wang, M. Cheng, Z. Bi, Y. Dong, H. Zhang, J. Zhang, et al., Structure and impedance of ZrO_2 doped with Sc_2O_3 and CeO_2, Mater. Lett. 59 (2005) 2579–2582, https://doi.org/10.1016/j.matlet.2004.07.065.

[31] F.A. Silva, D.S. Martinez, J.A.C. Ruiz, L.V. Mattos, C.E. Hori, F.B. Noronha, The effect of the use of cerium-doped alumina on the performance of Pt/CeO2/Al2O3 and Pt/$CeZrO_2$/$Al2O_3$ catalysts on the partial oxidation of methane, Appl. Catal. A-Gen. 335 (2008) 145–152, https://doi.org/10.1016/j.apcata.2007.11.003.

[32] W. Shan, M. Luo, P. Ying, W. Shen, C. Li, Reduction property and catalytic activity of $Ce_{1-x}Ni_xO_2$ mixed oxide catalysts for CH_4 oxidation, Appl. Catal. A-Gen. 246 (2003) 1–9, https://doi.org/10.1016/S0926-860X(02)00659-2.

[33] S.P. Padi, L. Shelly, E.P. Komarala, D. Schweke, S. Hayun, B.A. Rosen, Coke-free methane dry reforming over nano-sized NiO-CeO_2 solid solution after exsolution, Catal. Commun. 138 (2020), 105951, https://doi.org/10.1016/j.catcom.2020.105951.

[34] A. Abduraimova, A. Molkenova, A. Duisembekova, T. Mulikova, D. Kanayeva, T. S. Atabaev, Cetyltrimethylammonium bromide (CTAB)-Loaded SiO_2-Ag mesoporous nanocomposite as an efficient antibacterial agent, Nanomater 11 (2021) 477, https://doi.org/10.3390/nano11020477.

[35] F. Zhang, C. Chen, J.C. Hanson, R.D. Robinson, I.P. Herman, S. Chan, Phases in ceria-zirconia binary oxide (1-*x*)CeO_2-*x*ZrO_2 nanoparticles: the effect of particle size, J. Am. Ceram. Soc. 89 (2006) 1028–1036, https://doi.org/10.1111/j.1551-2916.2005.00788.x.

[36] G. Garbarino, S. Campodonicob, A.Romero Perez, M.M. Carnascialib, P. Rianib, E. Finocchio, G. Busca, Spectroscopic characterization of Ni/Al2O3 catalytic materials for the steam reforming of renewables, Appl. Catal. A-Gen. 452 (2013) 163–173, https://doi.org/10.1016/j.apcata.2012.10.039.

[37] G. Gouadec, P. Colomban, Raman Spectroscopy of nanomaterials: how spectra relate to disorder, particle size and mechanical properties, Prog. Cryst. Growth Charact. Mater. 53 (2007) 1–56, https://doi.org/10.1016/j.pcrysgrow.2007.01.001.

[38] A. Kambolis, H. Matralis, A. Trovarelli, C. Papadopoulou, Ni/CeO_2-ZrO_2 catalysts for the dry reforming of methane, Appl. Catal. A-Gen. 377 (2010) 16–26, https://doi.org/10.1016/j.apcata.2010.01.013.

[39] R. Sharan, A. Dutta, Structural analysis of Zr4+ doped ceria, a possible material for ammonia detection in ppm level, J. Alloy. Compd. 693 (2017) 936–944, https://doi.org/10.1016/j.jallcom.2016.09.267.

[40] P. Luches, S. Valeri, Structure, morphology and reducibility of epitaxial cerium oxide ultrathin films and nanostructures, Materials 8 (2015) 5818–5833, https://doi.org/10.3390/ma8095278.

[41] W. Dow, T. Huang, Yttria-stabilized zirconia supported copper oxide catalyst, J. Catal. 160 (1996) 171–182, https://doi.org/10.1006/jcat.1996.0135.

[42] Z. Song, P. Liu, Y. Fu, H. Liu, Z. Huang, H. Kang, Y. Mao, B. Liu, Y. Guo, Promotional effect of acidic oxide on catalytic activity and N_2 selectivity over CeO_2 for selective catalytic reduction of NO_x by NH_3, Appl. Organomet. Chem. 33 (2019), e4919, https://doi.org/10.1002/aoc.4919.

[43] B.M. Reddy, P.M. Sreekanth, P. Lakshmanan, A. Khan, Synthesis, characterization and activity study of $SO_4^{2-}/Ce_xZr_{1-x}O_2$ solid superacid catalyst, J. Mol. Catal. A Chem. 244 (2006) 1–7, https://doi.org/10.1016/j.molcata.2005.08.054.

[44] N. Rui, X. Zhang, F. Zhang, Z. Liu, X. Cao, Z. Xie, R. Zou, S.D. Senanayake, Y. Yang, J.A. Rodriguez, C.J. Liu, Highly active Ni/CeO_2 catalyst for CO_2 methanation: Preparation and characterization, Appl. Catal. B: Environ. 282 (2021), 119581, https://doi.org/10.1016/j.apcatb.2020.119581.

[45] J. Fan, X. Wu, X. Wu, Q. Liang, R. Ran, D. Weng, Thermal ageing of Pt on low-surface-area CeO_2-ZrO_2-La_2O_3 mixed oxides: Effect on the OSC performance, Appl. Catal. B: Environ. 81 (2008) 38–48, https://doi.org/10.1016/j.apcatb.2007.11.022.

[46] N. Weidler, J. Schuch, F. Knaus, P. Stenner, S. Hoch, A. Maljusch, R. Schafer, B. Kaiser, W. Jaegermann, X-ray photoelectron spectroscopic investigation of plasma-enhanced chemical vapor deposited NiO_x, $NiO_x(OH)_y$, and $CoNiO_x(OH)_y$: influence of the chemical composition on the catalytic activity for the oxygen evolution reaction, J. Phys. Chem. C. 121 (2017) 6455–6463, https://doi.org/10.1021/acs.jpcc.6b12652.

[47] Y. Kwon, J.E. Eichler, C.B. Mullins, $NiAl_2O_4$ as a beneficial precursor for Ni/Al_2O_3 catalysts for the dry reforming of methane, J. CO_2 Util. 63 (2022), 102112, https://doi.org/10.1016/j.jcou.2022.102112.

[48] Y. Wang, S. Aghamohammadi, D. Li, K. Li, R. Farrauto, Structure dependence of Nb_2O_{5-x} supported manganese oxide for catalytic oxidation of propane: enhanced oxidation activity for MnOx on a low surface area Nb_2O_{5-x}, Appl. Catal. B: Environ. 244 (2019) 438–447, https://doi.org/10.1016/j.apcatb.2018.11.066.

[49] B. Liu, C. Li, G. Zhang, X. Yao, S.S.C. Chuang, Z. Li, Oxygen vacancy promoting dimethyl carbonate synthesis from CO_2 and methanol over Zr-doped CeO_2 nanorods, ACS Catal. 8 (2018) 10446–10456, https://doi.org/10.1021/acscatal.8b00415.

[50] S. Tsunekawa, K. Asami, S. Ito, M. Yashima, T. Sugimoto, XPS study of the phase transition in pure zirconium oxide nanocrystallites, Appl. Surf. Sci. 252 (2005) 1651–1656, https://doi.org/10.1016/j.apsusc.2005.03.183.

[51] L.T. Do, C. Nguyen-Huy, E.W. Shin, Different metal support interactions over NiK/ mixed oxide catalysts and their effects on catalytic routes in steam catalytic cracking of vacuum residue, ChemistrySelect 3 (2018) 1827–1835, https://doi.org/10.1002/slct.201702819.

[52] D.A. Pawlak, M. Ito, M. Oku, K. Shimamura, T. Fukuda, Interpretation of XPS O (1s) in mixed oxides proved on mixed perovskite crystals, J. Phys. Chem. B. 106 (2002) 504–507, https://doi.org/10.1021/jp012040a.

[53] P.M. Shah, J.W.H. Burnett, D.J. Morgan, T.E. Davies, S.H. Taylor, Ceria-zirconia mixed metal oxides prepared via mechanochemical grinding of carbonates for the total oxidation of propane and naphthalene, Catalysts 9 (2019) 475, https://doi.org/10.3390/catal9050475.

[54] A. Caballero, J.P. Holgado, V.M. Gonzalez-de la Cruz, S.E. Habas, T. Herranz, M. Salmeron, In situ spectroscopic detection of SMSI effect in a Ni/CeO2 system: hydrogen-induced burial and dig out of metallic nickel, Chem. Comm. 46 (2010) 197–199, https://doi.org/10.1039/B920803H.

[55] R. Mane, C. Rode, Simultaneous glycerol dehydration and in situ hydrogenolysis over Cu-Al oxide under an inert atmosphere, Green. Chem. 14 (2012) 2780–2789, https://doi.org/10.1039/C2GC35661A.

[56] D. Goma, J.J. Delgado, L. Lefferts, J. Faria, J.J. Calvino, M.A. Cauqui, Catalytic performance of Ni/CeO_2/X-ZrO_2 (X = Ca, Y) catalysts in the aqueous-phase reforming of methanol, Nanomaterials 9 (2019) 1582, https://doi.org/10.3390/nano9111582.

[57] M.L. Ang, U. Oemar, E.T. Saw, L. Mo, Y. Kathiraser, B.H. Chia, S. Kawi, Highly active Ni/xNa/CeO_2 catalyst for the water-gas shift reaction: effect of sodium on methane suppression, ACS Catal. 4 (2014) 3237–3248, https://doi.org/10.1021/cs500915p.

[58] R. Ye, Q. Li, W. Gong, T. Wang, J.J. Razink, L. Lin, Y.Y. Qin, Z. Zhou, H. Adidharma, J. Tang, A.G. Russell, M. Fan, Y.G. Yao, High-performance of nanostructured Ni/CeO_2 catalyst on CO_2 methanation, Appl. Catal. B: Environ. 268 (2020), 118474, https://doi.org/10.1016/j.apcatb.2019.118474.

[59] G. Zhou, H. Liu, K. Cui, A. Jia, G. Hu, Z. Jiao, Y. Liu, X. Zhang, Role of surface Ni and Ce species of Ni/CeO_2 catalyst in CO_2 methanation, Appl. Surf. Sci. 383 (2016) 248–252, https://doi.org/10.1016/j.apsusc.2016.04.180.

[60] R.R. Davda, J.W. Shabaker, G.W. Huber, R.D. Cortright, J.A. Dumesic, A review of catalytic issues and process conditions for renewable hydrogen and alkanes by aqueous-phase reforming of oxygenated hydrocarbons over supported metal catalysts, Appl. Catal. B: Environ. 56 (2005) 171–186, https://doi.org/10.1016/j.apcatb.2004.04.027.

[61] S. Hilaire, X. Wang, T. Luo, R.J. Gorte, J. Wagner, A comparative study of Water-Gas-Shift reaction over ceria supported metallic catalysts, Appl. Catal. A-Gen. 215 (2004) 271–278, https://doi.org/10.1016/S0926-860X(01)00535-X.

[62] Y. Guo, M.U. Azmat, X. Liu, Y. Wang, G. Lu, Effect of support's basic properties on hydrogen production in aqueous-phase reforming of glycerol and correlation between WGS and APR, Appl. Energy 92 (2012) 218–223, https://doi.org/10.1016/j.apenergy.2011.10.020.

[63] Y. Nakagawa, K. Tomishige, Heterogeneous catalysis of the glycerol hydrogenolysis, Catal. Sci. Technol. 1 (2011) 179–190, https://doi.org/10.1039/C0CY00054J.

[64] J. Remón, J.R. Giménez, A. Valiente, L. García, J. Arauzo, Production of gaseous and liquid chemicals by aqueous phase reforming of crude glycerol: Influence of operating conditions on the process, Energy Convers. Manag. 110 (2016) 90–112, https://doi.org/10.1016/j.enconman.2015.11.070.

[65] T. Jiang, D. Kong, K. Xu, F. Cao, Hydrogenolysis of glycerol aqueous solution to glycols over Ni-Co bimetallic catalyst: effect of ceria promoting, Appl. Petrochem. Res. 6 (2016) 135–144, https://doi.org/10.1007/s13203-015-0128-8.

[66] A. Syuhada, M. Ameen, M.T. Azizan, A. Aqsha, M.H.M. Yusoff, A. Ramli, M. Sahban, F. Sher, In-situ hydrogenolysis of glycerol using hydrogen produced via aqueous phase reforming of glycerol over sonochemically synthesized nickel-based nano-catalyst, Mol. Catal. 514 (2021), 111860, https://doi.org/10.1016/j.mcat.2021.111860.

[67] I. Gandarias, P.L. Arias, J. Requies, M.B. Güemez, J.L.G. Fierro, Hydrogenolysis of glycerol to propanediols over a Pt/ASA catalyst: The role of acid and metal sites on product selectivity and the reaction mechanism, Appl. Catal. B: Environ. 97 (2010) 248–256, https://doi.org/10.1016/j.apcatb.2010.04.008.

[68] E.S. Vasiliadou, E. Heracleous, I.A. Vasalos, A.A. Lemonidou, Ru-based catalysts for glycerol hydrogenolysis-effect of support and metal precursor, Appl. Catal. B: Environ. 92 (2009) 90–99, https://doi.org/10.1016/j.apcatb.2009.07.018.

[69] B. Liu, J. Greeley, A density functional theory analysis of trends in glycerol decomposition on close-packed transition metal surfaces, Phys. Chem. Chem. Phys. 15 (2013) 6475–6485, https://doi.org/10.1039/C3CP44088E.

[70] S. Jeon, H. Roh, D. Moon, J. Bae, Aqueous phase reforming and hydrodeoxygenation of ethylene glycol on Pt/SiO_2-Al_2O_3: effects of surface acidity on product distribution, RSC Adv. 6 (2016) 68433–68444, https://doi.org/10.1039/C6RA09522D.

[71] J. Huo, J. Tessonnier, B.H. Shanks, Improving hydrothermal stability of supported metal catalysts for biomass conversions: a review, ACS Catal. 11 (2021) 5248–5270, https://doi.org/10.1021/acscatal.1c00197.

[72] J. Duan, Y.T. Kim, H. Lou, G.W. Huber, Hydrothermally stable regenerable catalytic supports for aqueous-phase conversion of biomass, Catal. Today 234 (2014) 66–74, https://doi.org/10.1016/j.cattod.2014.03.009.

[73] A.G. Chakinala, J.K. Chinthaginjala, K. Seshan, W.P.M. van Swaaij, S.R.A. Kersten, D.W.F. Brilman, Catalyst screening for the hydrothermal gasification of aqueous phase of bio-oil, Catal. Today 195 (2012) 83–92, https://doi.org/10.1016/j.cattod.2012.07.042.

[74] A. Morales-Marín, J.L. Ayastuy, U. Iriarte-Velasco, M.A. Gutiérrez-Ortiz, Nickel aluminate spinel-derived catalysts for the aqueous phase reforming of glycerol: effect of reduction temperature, Appl. Catal. B: Environ. 244 (2019) 931–945, https://doi.org/10.1016/j.apcatb.2018.12.020.

[75] S. Jeon, Y.M. Park, K. Saravanan, G.Y. Han, B. Kim, J. Lee, J.W. Bae, Aqueous phase reforming of ethylene glycol over bimetallic platinum-cobalt on ceria-zirconia mixed oxide, Int. J. Hydrog. Energy 42 (2017) 9892–9902, https://doi.org/10.1016/j.ijhydene.2017.01.221.

[76] A.J. Reynoso, U. Iriarte-Velasco, M.A. Gutiérrez-Ortiz, J.L. Ayastuy, Highly stable Pt/$CoAl_2O_4$ catalysts in aqueous-phase reforming of glycerol, Catal. Today 367 (2021) 278–289, https://doi.org/10.1016/j.cattod.2020.03.039.

[77] S.N.A. Rosli, S.Z. Abidin, O.U. Osazuwa, X. Fan, Y. Jiao, The effect of oxygen mobility/vacancy on carbon gasification in nano catalytic dry reforming of

methane: a review, J. CO_2 Util. 63 (2022), 102109, https://doi.org/10.1016/j.jcou.2022.102109.

[78] T. Van Haasterecht, C.C.I. Ludding, K.P. De Jong, J.H. Bitter, Toward stable nickel catalysts for aqueous phase reforming of biomass-derived feedstock under reducing and alkaline conditions, J. Catal. 319 (2014) 27–35, https://doi.org/10.1016/j.jcat.2014.07.014.

[79] M. Besson, P. Gallezot, Deactivation of metal catalysts in liquid phase organic reactions, Catal. Today 81 (2003) 547–559, https://doi.org/10.1016/S0920-5861(03)00153-6.